JOURNAL OF GEOPHYSICAL RESEARCH: SOLID EARTH, VOL. 118, 71–82, doi:10.1029/2012JB009615, 2013

Analytical solutions and numerical tests of elastic and failure behaviors of close-packed lattice for brittle rocks and crystals

Chun Liu,[1] David D. Pollard,[2] and Bin Shi[1]

Received 9 July 2012; revised 31 October 2012; accepted 31 October 2012; published 30 January 2013.

[1] Analytical solutions of elastic properties and failure modes of a two-dimensional close-packed discrete element model are proposed. Based on the assumption of small deformation, the conversion formulas between five inter-particle parameters of the lattice model and rock mechanical properties were derived. Using the formulas, the inter-particle parameters can be determined by Young's modulus (E), Poisson's ratio (v), tensile strength (T_u), compressive strength (C_u), and coefficient of intrinsic friction (μ_i). The lattice defined by the parameters simulates the elastic and failure behaviors of rocks and crystals and therefore can be used to investigate the initiation and development of geological structures quantitatively. Furthermore, the solutions also provide a theoretical basis for the calibration of parameters of random discrete assemblies. The model of quartz was used as an example to validate the formulas and test the errors. The simulated results show that E and v converge to theoretical values when particle number increases. These elastic properties are almost constant when the magnitude of strain is lower than 10^{-3}. The simulated T_u and C_u of a single three-element unit are also consistent with the formulas. However, due to the boundary effects and stress concentrations, T_u and C_u of lattices with multiple units are lower than the values predicted by the formulas. Therefore, greater T_u and C_u can be used in the formulas to counteract this effect. The model is applicable to the simulation of complicated structures that involve deformation and failure at different scales.

Citation: Liu, C., D. D. Pollard, and B. Shi (2013), Analytical solutions and numerical tests of elastic and failure behaviors of close-packed lattice for brittle rocks and crystals, *J. Geophys. Res. Solid Earth*, *118*, 71–82, doi: 10.1029/2012JB009615.

1. Introduction

[2] The discrete element method (DEM) [*Mora and Place*, 1993, 1994; *Place et al*., 2002] is based on molecular dynamics and was first developed in the fields of physics and fluid dynamics [*Hoover et al*., 1974]. The method has been demonstrated to be a powerful numerical tool since Cundall and Strack [1979] introduced it to study the behavior of granular assemblies. In the method, the granular assemblies are made up of a series of soft particles, which obey Newton's equations of motion. The mechanical, physical and chemical behaviors can be simulated by investigating the movement of the discrete assemblies. The method has been used to simulate the behaviors of granular materials [*Kuhn*, 1999; *Morgan and Boettcher*, 1999; *Kuhn and Bagi*, 2004; *Ergenzinger et al*., 2011]. Furthermore, it is an effective way to validate the predictions of continuum mechanics [*Wensrich and Stratton*, 2011] and can be combined with traditional continuum methods, such as FEM [*Nitka et al*., 2011].

[3] Most media are discontinuous at some level of observation, where the continuum assumptions cease to apply [*Griffith*, 1921]. Discontinuities can be pre-existing, such as bedding planes, lithologic interfaces, and flaws, or they can form during tectonic events, such as faulting and fracturing. For problems with significant deformation and breakage, the DEM is more convenient and powerful, since it permits large relative motion inside the model and dynamic evolution [*Hazzard et al*., 2000; *Boutt and McPherson*, 2002] and does not require re-meshing, for example, as finite element method [*Tradegard et al*., 1998; *Mei et al*., 1999; *Paluszny and Matthai*, 2009]. Therefore, the DEM has been widely used in the simulation and interpretation of various geological structures that involve breakage and discontinuities, such as deformation bands [*Antonellini and Pollard*, 1995; *Wang et al*., 2008], the reactivation of basement faults [*Saltzer and Pollard*, 1992], faulting over active salt diapir [*Yin et al*., 2009], detachment folding [*Hardy and Finch*, 2005], growth fault bend folding [*Benesh et al*., 2007], fault propagation folding [*Finch et al*., 2003; *Hardy and Finch*, 2006, 2007], and syn-tectonic sedimentation [*Carmona et al*., 2010].

[4] A major issue with the application of the DEM for geological investigations is the determination of the model parameters, such as stiffness and inter-particle breaking strain [*Mora and Place*, 1994; *Finch et al*., 2003]. In some previous studies, the physical properties (mass, density) and mechanical parameters (stiffness, breaking force) of

[1]School of Earth Sciences and Engineering, Nanjing University, Nanjing China.
[2]Department of Geological and Environmental Sciences, Stanford University, Stanford California, USA.

Corresponding author: C. Liu, School of Earth Sciences and Engineering, Nanjing University, 22 Hankou Rd., Nanjing 210093, China. (oxtown@gmail.com)

2169-9313/13/2012JB009615

particles of the discrete element model were usually given in non-dimensionalized model units and were set to unity [*Mora and Place*, 1994; *Yin et al*., 2009]. However, the results of such numerical simulations are qualitative, lacking clues about the mechanical properties of the model and the form of structures. Therefore, in order to quantify the influence of rock mechanical properties on the development of structures, it is necessary to define the model parameters according to the real rock properties. Then, by varying the parameters and running a simulation to reproduce the geological phenomenon, geologists can explore the relationship between the rock properties and the development of structures.

[5] As for an assemblage of random discrete particles with polydisperse size distribution and/or random packing, a general method is to do a simulation and determine the effective mechanical properties such as Poisson's ratio, Young's modulus, uniaxial compressive strength, etc. [*Boutt and McPherson*, 2002; *Potyondy and Cundall*, 2004; *Hardy et al*., 2007; *Roul et al*., 2011]. The modeling method relies on calibration processes to determine the correct inter-particle parameters. Via the calibration operations, *Kazerani and Zhao* [2010] demonstrated that macro-mechanical properties of material (i.e. Young's modulus, Poisson's ratio, internal friction angle, internal cohesion, and tensile strength) directly originate from and therefore are related to micro inter-particle parameters (i.e., normal and shear stiffness, coefficient of friction, cohesion, and tensile strength). *Tavarez and Plesha* [2007] investigate the Young's modulus and Poisson's ratio of close-packed discrete element model. The close-packed model has analytical elastic solutions [*Griffiths and Mustoe*, 2001], which can be verified by numerical tests. However, the relationships between the material properties and inter-particle parameters are still not clear. And it is difficult to define an assemblage with specified mechanical properties of rocks, such as compressive strength and coefficient of intrinsic friction, and perform similar failure behaviors as a real material.

[6] The elastic properties and failure modes of a regular close-packed discrete element model is investigated in this study. In the model, rock is represented by bonded particles, of which the inter-particle behaviors are defined by five parameters: normal stiffness (K_n), shear stiffness (K_s), breaking displacement (X_b), shear resistance (Fs_0), and coefficient of friction (μ_p). Based on the assumption of small deformation, a basic unit with three particles was used to explore the dependence of rock mechanical properties on the inter-particle parameters. The conversion formulas between the five inter-particle parameters and five mechanical properties of the lattice was derived, including Young's modulus (E), Poisson's ratio (v), tensile strength (T_u), compressive strength (C_u), and coefficient of intrinsic friction (μ_i). Then, the model of a quartz grain was used as an example to validate the formulas. A series of numerical tests were conducted to investigate the error and convergence of the model during elastic deformation and brittle failure. Finally, the application of the model is discussed.

2. Discrete Element Model

2.1. The Basic Lattice Model

[7] The discrete element model used here is based on the lattice model, which was used to simulate the dynamical processes associated with earthquakes [*Mora and Place*, 1993, 1994]. Recently, the model was applied to investigate the kinematic characteristics of structures [*Hardy and Finch*, 2006; *Yin et al*., 2009]. The discontinuous methods use a series of elastic particles (i.e., two-dimensional disks) which obey Newton's equations of motion. The particles of the model are bonded by breakable elastic springs, and the force can occur only at point contacts between neighboring particles (Figures 1a and 1b).

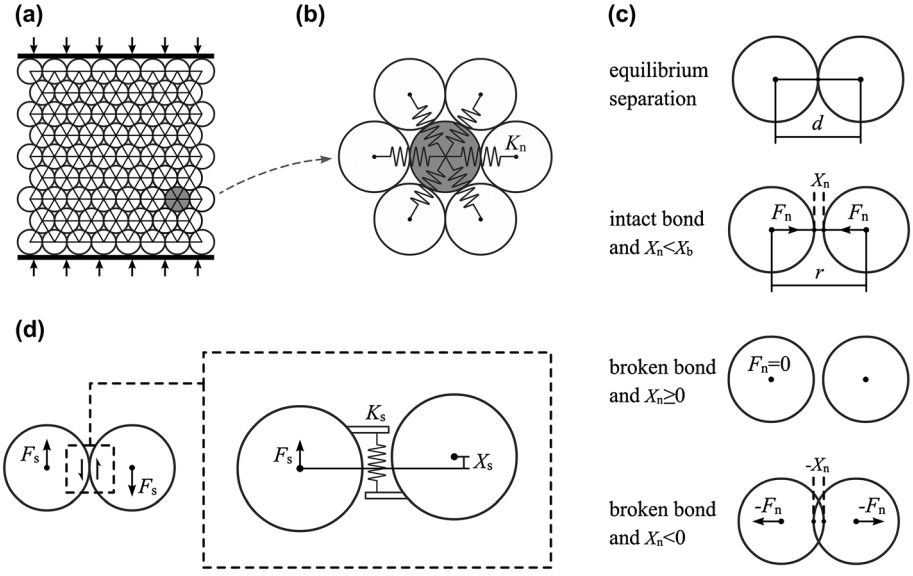

Figure 1. (a) The two-dimensional close-packed lattice. (b) A central particle is bonded by six neighboring particles, which interact through a spring force. (c) The spring between two particles will break when the normal relative displacement X_n exceeds the breaking displacement X_b, and the tensile force will not exist between them. (d) Similarly, two particles are bonded by breakable elastic spring along the tangential direction to simulate the shear deformation and shear force (see text).

[8] In the model discussed in this paper, particles with the same radius are close packed (Figure 1a), that is, the hexagonal lattice. The particles interact through a "repulsive-attractive" spring force in which the normal force between two particles, F_n, is given by

$$F_n = K_n X_n \tag{1}$$

where K_n is the normal spring stiffness of the bond; X_n is the normal relative displacement. As shown in Figure 1c, X_n equals the current inter-particle separation (r) minus the particle diameter (d). Particles are bonded to their neighbors, and experience an attractive or repulsive force, until X_n between the particle pair exceeds the breaking displacement X_b (Figure 1c). The maximum inter-particle normal force (F_{nmax}) is

$$F_{nmax} = K_n X_b \quad \text{intact bond} \tag{2}$$

[9] Then, the bond is broken in opening mode and the tensile force ceases to exist between them.

[10] However, the repulsive force still acts between the two particles when they return to a compressive contact (Figure 1c):

$$F_n = K_n X_n \quad X_n < 0, \text{broken bond} \tag{3}$$

2.2. Shear Force and Shear Resistance

[11] In addition to the normal force (F_n), the shear (tangential) force, F_S, is also considered [*Cundall and Strack*, 1979; *Place and Mora*, 1999; *Hardy et al*., 2009]. As shown in Figure 1d, when two particle surfaces are in contact and slipping past one another, a dynamic frictional force opposes the direction of slip. It is assumed that the two particles are also bonded by breakable elastic springs along the tangential direction, and the force (F_S) of the shear spring is determined by

$$F_S = K_s X_s \tag{4}$$

where K_s is the shear stiffness and X_s is the tangential relative displacement between the two particles. For an intact bond, the maximum shear force (F_{Smax}) allowed by Coulomb friction is

$$F_{Smax} = F_{S0} - \mu_p F_n \quad \text{intact bond} \tag{5}$$

where F_{S0} is the inter-particle shear resistance, μ_p is the inter-particle coefficient of friction, and F_n is the normal force (compressive force is negative). The intact bond between two particles will break when the external force exceeds the maximum shear force determined by equation (5). Then, the intact bond breaks and the inter-particle shear resistance (F_{S0}) will not exist between them. The magnitude of the shear force (F_S) is limited to be less than or equal to the maximum shear force of the broken bond:

$$F_{Smax} = -\mu_p F_n \quad \text{broken bond} \tag{6a}$$

$$F_S = F_{Smax} (\text{if } F_S > F_{Smax}) \tag{6b}$$

[12] In the case of broken bond, two particles begin slipping when the magnitude of external force exceeds the maximum shear force determined by equation (6a); when two particles separate from each other ($X_n > 0$), the normal force and shear force between the particles are set to zero.

2.3. Numerical Solution

[13] In numerical simulations, an artificial viscosity (F_v) is added to damp the reflected waves from the boundary of the particle and to avoid buildup of kinetic energy in the closed system [*Mora and Place*, 1993, 1994; *Place et al*., 2002; *Finch et al*., 2003]. The viscous force is proportional to the particle velocities and is given by

$$F_v = -\eta \cdot x' \tag{7}$$

where η is the artificial viscosity and x' is the particle velocity.

[14] The resultant force acting on a particle is the summation of all the forces on each bond that links the particle to its neighbors and the viscous force. The dynamic evolution of an assemblage can be modeled and observed by a time-stepping algorithm [*Cundall and Strack*, 1979; *Potyondy and Cundall*, 2004]. Assuming that the motion of the particles is linear during a very small time step, then the resultant force, acceleration, velocity, and displacement of the particles can be calculated during the time step [*Mora and Place*, 1993, 1994]. The particles are advanced to their new positions by integrating their equations of motion using Newtonian physics. The details about the numerical simulations will be introduced in section 5.

3. Elastic Properties of Close-Packed Lattice

[15] The close-packed lattice (regular hexagonal packing) shown in Figure 1a is composed of particles with identical size and inter-particle mechanical parameters. The mechanical properties of the model depend on the mechanical parameters of the particles, when the layout of the particles is determined. The discrete element model introduced in section 2 involves the following five independent inter-particle parameters: normal stiffness (K_n), shear stiffness (K_s), breaking displacement (X_b), shear resistant (Fs_0), and coefficient of friction (μ_p). In this section, the parameters are used to define the mechanical properties of the close-packed lattice, such as Young's modulus (E), shear modulus (G), and Poisson's ratio (v), etc.

3.1. Deformation of Basic Triangular Unit

[16] The basic triangular unit of the close-packed lattice shown in Figure 2 is used to investigate the mechanical properties of the lattice on the basis of the small deformation assumption, in which the displacement of particles is very small, so the deformation of the unit is assumed to be linear. In the unit, the three particles are bonded to each other by three intact bonds (bonds 1–3). Since all the particles have the same diameter (d), the triangle ABC is an equilateral triangle. The y coordinate of particles 2 and 3 is fixed. An external force, Fy, acts on particle 1, which moves upward by a very small displacement dy. The angle $A'BC$ and angle $A'CB$ are still 60°. Since the model is symmetrical around the y axis, the external forces acting on particles 2 and 3 (Fy_2 and Fy_3 in Figure 2) equals $0.5Fy$.

[17] Equilibrium condition of particle 1 requires that the normal force (F_{n1}) between particles 1 and 2 is tensile

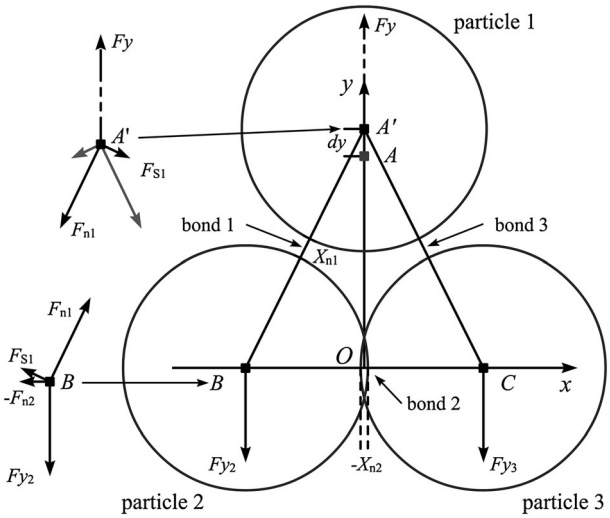

Figure 2. A vertical force Fy acts on a three-particle unit. The deformation of the basic triangular unit is used to investigate the mechanical properties of the lattice model.

(positive) and consequently the normal relative displacement (X_{n1}) is positive. Similarly, particles 2 and 3 move toward the point O, and the normal relative displacement between them is negative. According to equations (1) and (4), the normal and shear forces between particles can be defined as follows (physical equations):

$$\begin{cases} F_{n1} = K_n \cdot X_{n1} \\ F_{S1} = K_s \cdot X_{s1} \\ F_{n2} = K_n \cdot X_{n2} \end{cases} \tag{8}$$

where F_{n1} and F_{S1} are, respectively, the normal and shear forces between particles 1 and 2 (bond 1), F_{n2} is the normal force between particles 2 and 3 (bond 2), and the right sides of the equations are the corresponding stiffness and relative displacements. The forces acting on particles 1 and 2 are shown in Figure 2. The balance equations of particle 1 along y axis and particle 2 along x axis are

$$\begin{cases} Fy = \sqrt{3} \cdot F_{n1} + F_{S1} \\ -F_{n2} = 1/2 \cdot F_{n1} - \sqrt{3}/2 \cdot F_{S1} \end{cases} \tag{9}$$

[18] The normal and shear displacements between particles 1 and 2 are related to dy and X_{n2} as (geometric equations)

$$\begin{cases} X_{n1} = \sqrt{3}/2 \cdot dy + 1/4 \cdot X_{n2} \\ X_{s1} = 1/2 \cdot dy - \sqrt{3}/4 \cdot X_{n2} \end{cases} \tag{10}$$

[19] In equations (8)–(10), Fy, K_n, and K_s are known. There are seven unknown variables in the seven equations. Therefore, the equations can be solved, and dy, X_{n1}, X_{s1}, and X_{n2} are

$$dy = \frac{3K_n + K_s}{4K_n(K_n + K_s)} \cdot Fy \tag{11a}$$

$$X_{n1} = \frac{\sqrt{3}(2K_n + K_s)}{6K_n(K_n + K_s)} \cdot Fy \tag{11b}$$

$$X_{s1} = \frac{1}{2(K_n + K_s)} \cdot Fy \tag{11c}$$

$$X_{n2} = -\frac{\sqrt{3}(K_n - K_s)}{6K_n(K_n + K_s)} \cdot Fy \tag{11d}$$

[20] The equations will be used to derive the elastic properties and strengths of the unit in the following sections.

3.2. Young's Modulus, Shear Modulus, and Poisson's Ratio

[21] In the basic triangle unit, the normal stresses along the x direction (σ_{xx}) and y direction (σ_{yy}) are (tensile stress is positive)

$$\begin{cases} \sigma_{xx} = 0 \\ \sigma_{yy} = Fy/d \end{cases} \tag{12}$$

where Fy is the vertical force acting on the triangle unit; d is the particle diameter. With the equations and equations (11a) and (11d), the normal strains of the unit along x direction (ε_{xx}) and y direction (ε_{yy}) are given as

$$\varepsilon_{xx} = \frac{X_{n2}}{l_{BC}} = -\frac{\sqrt{3}(K_n - K_s)}{6K_n(K_n + K_s)} \cdot \sigma_{yy} \tag{13a}$$

$$\varepsilon_{yy} = \frac{dy}{l_{AO}} = \frac{\sqrt{3}(3K_n + K_s)}{6K_n(K_n + K_s)} \cdot \sigma_{yy} \tag{13b}$$

where l_{BC} and l_{AO} are the lengths of segments BC and AO (Figure 2), respectively. The model is two dimensional, and the normal in-plane stresses in the x and y directions are [*Pollard and Fletcher*, 2005, p. 299]

$$\begin{cases} \sigma_{xx} = (2G + \lambda)\varepsilon_{xx} + \lambda\varepsilon_{yy} \\ \sigma_{yy} = \lambda\varepsilon_{xx} + (2G + \lambda)\varepsilon_{yy} \end{cases} \tag{14}$$

where G is the shear modulus; λ is Lame's constant. The stress-strain relations in equation (14) assume conditions of plane strain ($\varepsilon_{zz} = 0$). Substituting equations (12) and (13a)–(13b) into equation (14), the shear modulus and Lame's constant are

$$G = \sqrt{3}/4 \cdot (K_n + K_s) \tag{15}$$

$$\lambda = \sqrt{3}/4 \cdot (K_n - K_s) \tag{16}$$

[22] Then, the Young's modulus (E) and Poisson's ratio (v) can be derived from the shear modulus and Lame's constant:

$$E = \sqrt{3}(K_n + K_s) \cdot (5K_n - K_s)/(8K_n) \tag{17}$$

$$v = 1/4 \cdot (1 - K_s/K_n) \tag{18}$$

[23] Dividing equations (15)–(17) by K_n, the right sides of the expressions are only determined by the ratio of shear stiffness to normal stiffness (γ). The results and Poisson's ratio are plotted versus γ in Figure 3. If K_n is assumed to be one unit, the figure indicates that the Young's modulus (E) and shear modulus (G) increase with increasing K_s, while the Lame's constant (λ) and Poisson's ratio decreases linearly with increasing K_s. The theoretical range of Poisson's ratio in the generalized Hooke's law for an isotropic continuum is from -1.0 to 0.5 [*Lakes*, 1987; *Bathurst and Rothenburg*,

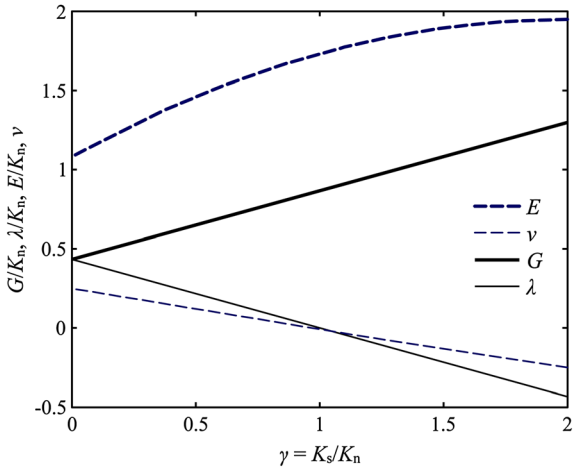

Figure 3. Relationships between elastic properties (G, λ, E, and ν) of close-packed model and the normal stiffness (K_n) and shear stiffness (K_s).

1988]. Since the normal stiffness (K_n) and shear stiffness (K_s) cannot be negative, the maximum Poisson's ratio of the close-packed lattice is 0.25 when γ is 0. When $\gamma = 1$, this corresponds to a material with Poisson's ratio equal zero. When $\gamma > 1$, Poisson's ratio is negative, which implies the material has the unusual property of narrowing when compressed. This state of affairs occurs when the tangential interaction is stiffer than the normal interaction [*Gaspar*, 2010].

[24] Equations (17) and (18) are consistent with the simulated results of previous works [Hazzard et la., 2000; *Boutt and McPherson*, 2002] that Young's modulus increases with increasing normal stiffness and the ratio of the shear to normal stiffness (γ) influences the Poisson's ratio. The Poisson's ratio of rocks and crystals is generally between 0.1 and 0.25; as a result, the corresponding range of γ is 0–0.6. However, for assemblies of random discrete particles, the Poisson's ratio versus γ curve is controlled by the compactness of the assemblage, reflected in the porosity and coordination number [*Kruyt and Rothenburg*, 2004]. The K_s/K_n ratio could be greater than 0.6. For example, $K_s = K_n$ was used in the simulation of the micro-mechanics of compaction localization in a granular rock [*Wang et al.*, 2008].

[25] In conclusion, the macro-elastic properties of the close-packed model are determined by the normal stiffness (K_n) and shear stiffness (K_s) of the particles [*Hazzard et al.*, 2000]. Specifically, if the shear stiffness is not considered ($K_s = 0$), the particular values of the solutions coincide with the results of previous studies [Hoover, 1974; *Mora and Place*, 1993]. Using a different approach based on strain energy density, *Griffiths and Mustore* [2001] also obtained similar results to equations (17) and (18). However, the new method based on small deformation has inherent advantages in the investigation of the failure modes of the lattice, which will be introduced in the following section.

4. Failure Modes of Close-Packed Lattice

[26] According to equations (2) and (5), an intact bond can be broken in opening mode or sliding mode, when the normal force or shear force exceeds the limits. Failure in tension and in shear may be defined using plots of a failure surface in coordinates of shear force (F_S) versus normal force (F_n). The inter-particle failure envelope determined by the equations is illustrated in Figure 4. In the gray region, the force states are impossible because of failure. The white region under the inter-particle failure envelope corresponds to possible force state. The inter-particle breaking displacement is very small, and deformation of the lattice is linear. Therefore, the force state path of an intact bond is generally a straight line, which starts at the origin and ends at the inter-particle failure envelope, where the intact bond breaks. As shown in Figure 4, bonds may break at points P_1 and P_2 in opening mode and sliding mode, respectively. The inter-particle failure envelope can be used to derive the tensile strength and compressive strength of the lattice model.

4.1. Tensile Strength

[27] Extension fractures typically appear when rock fails under uniaxial tension. The main characteristic of this type of fracture is a clean separation of the two halves of the sample, with no tangential offset between the two surfaces. In the triangle unit of Figure 2, with increasing tensile force Fy, the normal force (F_{n1}) and shear force (F_{S1}) of bond 1 increase. The corresponding force state point (Figure 4) moves from point O, along the segment OP_1, until reaching point P_1, where the bond breaks in opening mode. The tensile strength of the model (T_u) is defined as

$$T_u = \frac{Fy_b}{d} \tag{19}$$

where Fy_b is the vertical force when bond 1 breaks. Substituting equation (11b) into this equation gives the following expression for T_u:

$$T_u = \frac{2\sqrt{3}K_n(K_n + K_s)}{2K_n + K_s} \cdot \frac{X_b}{d} \tag{20}$$

where X_b is the inter-particle breaking displacement. Substituting the equation into equation (13b) ($\sigma_{yy} = T_u$), the tensile breaking strain (ε_t) can be expressed as

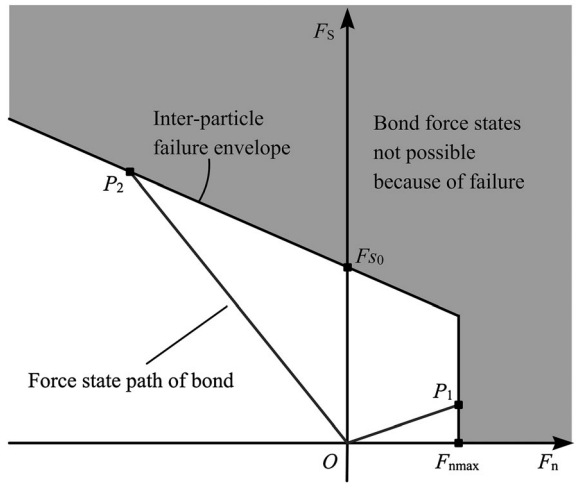

Figure 4. Shear-normal force space of a bond. Force state path of a bond starts at the origin O, along a straight line, until reaching the inter-particle failure envelope, where the bond breaks in opening mode (P_1) or sliding mode (P_2).

$$\varepsilon_t = \frac{3K_n + K_s}{2K_n + K_s} \cdot \frac{X_b}{d} \tag{21}$$

[28] The tensile breaking strain is related to the inter-particle breaking displacement (X_b). *Mora and Place* [1994] tested the parameters and showed that breaking strains for most materials were typically much less than 0.11. *Finch et al.* [2003] investigated the effect of the breaking separation and showed that large values of the breaking strain are associated with "strong" materials, which fail by localized faulting, whereas low values are associated with "weak" materials which deform in a macroscopically ductile manner.

4.2. Compressive Strength

[29] Microscopic observation of laboratory rock and crystal samples has shown that most cracks that form during compressive tests are tensile and sub-parallel to the maximum compressive stress [*Hallbauer et al.*, 1973; *Moore and Lockner*, 1995]. Experimental tests also show that shear fractures typically do not propagate in their own plane, and the eventual failure of the sample must occur by linking up of the tensile cracks to form a macro-shear fault [*Horii and Nemat-Nasser*, 1985]. When we consider failure of the lattice, the appearance of tensile cracks corresponds to the breakage of horizontal bonds [*Malan and Napier*, 1995; *Hazzard et al.*, 2000], which also has an analytical solution.

4.2.1. Opening Mode of Micro-cracks

[30] As shown in Figure 5, bond 2 breaks in opening mode when the relative displacement between particles 2 and 3 (X_{n2}) exceeds the breaking displacement (X_b). Let C_{open} represents the absolute value of the vertical stress when the bond breaks in opening mode. Substituting $X_{n2} = X_b$ into equation (13a), C_{open} can be expressed as

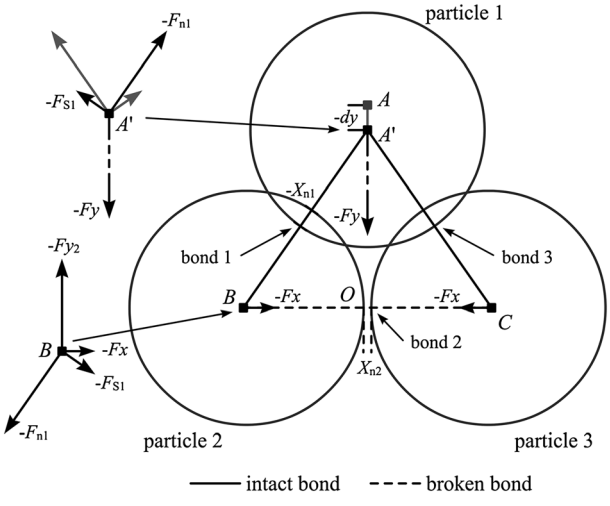

Figure 5. Bond 2 breaks when the relative displacement (X_{n2}) between particles 2 and 3 exceeds the breaking displacement (X_b). A vertical compressive force *Fy* and a horizontal compressive force *Fx* (negative) act on the triangle unit. The force states are used to derive the sliding mode of the fracture plane (see section 4.2.2).

$$C_{open} = -\sigma_{yy} = \frac{2\sqrt{3}K_n(K_n + K_s)}{(K_n - K_s)} \cdot \frac{X_b}{d} \tag{22}$$

[31] Combining equations (18), (20), and (22) gives the following equation between C_{open} and T_u:

$$C_{open}/T_u = (0.75/v - 1) \tag{23}$$

[32] The equation shows that the ratio of C_{open} to T_u is related to the Poisson's ratio (v). When $v = 0.25$ ($K_s = 0$), the first tensile crack appears when the magnitude of the vertical stress exceeds two times of the tensile strength, and the tensile crack does not occur in material with zero Poisson's ratio (when $K_s = 1$), since the material will not dilate laterally. The Poisson's ratio of rock is generally between 0.1 and 0.25. The corresponding ratio of C_{open}/T_u is between 2 and 6.5.

4.2.2. Sliding Mode of Fracture Plane

[33] In Figure 5, when bond 2 of the unit breaks, the tensile force between particles 2 and 3 will not exist. The failure of bond 1 corresponds to the macroscopic shear fracture plane of laboratory specimens. As shown in Figure 5, a vertical compressive force *Fy* and a horizontal compressive force *Fx* (negative) act on particles 1 and 2 (also on particle 3), respectively. The normal force (F_{n1}) and shear force (F_{S1}) of bond 1 can be expressed as (details in Appendix A)

$$\begin{cases} F_{n1} = \sqrt{3}/4 \cdot Fy + 1/2 \cdot Fx \\ F_{S1} = 1/4 \cdot Fy - \sqrt{3}/2 \cdot Fx \end{cases} \tag{24}$$

[34] According to equation (5), bond 1 will break when the magnitude of F_{S1} (negative) is equal to the maximum shear force allowed by Coulomb friction. Substituting equation (24) to equation (5) gives the following expression between *Fy* and *Fx*:

$$Fy = -\frac{4}{1 - \sqrt{3}\mu_p} \cdot F_{S0} + \frac{2\sqrt{3} + 2\mu_p}{1 - \sqrt{3}\mu_p} \cdot Fx \tag{25}$$

where μ_p and F_{S0} are inter-particle coefficient of friction and shear resistant, respectively. The normal stresses along the x direction (σ_{xx}) and y direction (σ_{yy}) are determined by

$$\begin{cases} \sigma_{xx} = 2\sqrt{3}/3 \cdot (Fx/d) \\ \sigma_{yy} = Fy/d \end{cases} \tag{26}$$

where d is particle diameter. Combined with equation (25), the relationship between σ_{xx} and σ_{yy} is

$$\sigma_{yy} = -\frac{4}{1 - \sqrt{3}\mu_p} \cdot \frac{F_{S0}}{d} + \frac{3 + \sqrt{3}\mu_p}{1 - \sqrt{3}\mu_p} \cdot \sigma_{xx} \tag{27}$$

[35] The equation defines the failure envelope of the unit in the stress-strain space, and the coefficient of σ_{xx} is the slope of the failure envelope. Therefore, the inter-particle coefficient of friction (μ_p) controls the slope of the Mohr-Coulomb failure envelope of the lattice, which has been demonstrated in previous numerical tests [*Boutt and McPherson*, 2002]. According to the Coulomb criterion, the stress state on the failure surface meets the following condition [*Pollard and Fletcher*, 2005, p. 363]:

$$\sigma_{yy} = -C_u + \left[\left(1+\mu_i^2\right)^{1/2} + \mu_i\right]^2 \sigma_{xx} \tag{28}$$

where C_u is the uniaxial compressive strength; μ_i is the coefficient of intrinsic friction. It is assumed that the Coulomb criterion is valid throughout the lattice. Then, the first and second terms of equation (27) are equal to those of equation (28), and the C_u and μ_i can be defined by

$$C_u = \frac{4}{1-\sqrt{3}\mu_p} \cdot \frac{F_{S0}}{d} \tag{29}$$

$$\mu_i = \frac{P-1}{2\sqrt{P}}, P = \frac{3+\sqrt{3}\mu_p}{1-\sqrt{3}\mu_p} \tag{30}$$

[36] Equation (29) indicates that inter-particle coefficient of friction (μ_p) must be lower than $\sqrt{3}/3$, as C_u is positive. According to equation (30), the lowest μ_i of the close-packed lattice is $\sqrt{3}/3$ when μ_p is 0. Note that $\sqrt{3}/3$ is the cotangent of 60°, and the lowest μ_i represents the intrinsic friction derived from the geometry of the equilateral triangle unit. The μ_i of rock and crystal is generally lower than 2, and the corresponding range of μ_p is from 0 to 0.455. The coefficient of intrinsic friction of the model (μ_i) is much greater than the inter-particle coefficient of friction (μ_p), due to the rough surface (geometry) of close-packed lattice [*Mora and Place*, 1994; *Place and Mora*, 1999]. A greater μ_p has been used in an assemblage of random discrete particles [*Hazzard et al*., 2000] ($\mu_p = 0.7$), as the intrinsic friction of the random assemblage derived from the geometry is smaller than that of the close-packed lattice. However, in the simulation of failure of particle aggregates, μ_p must be lower than $\sqrt{3}/3$. Otherwise, some particle aggregates in the random assemblage may have a negative C_u according to equation (29) and will not fail under compressive force.

[37] The shear strength of the lattice (S_0) can be defined by C_u and μ_i as [*Pollard and Fletcher*, 2005, p. 363]

$$S_0 = \frac{C_u}{2\left[\left(1+\mu_i^2\right)^{1/2} + \mu_i\right]} = \frac{2}{\sqrt{\left(3+\sqrt{3}\mu_p\right)\cdot\left(1-\sqrt{3}\mu_p\right)}} \cdot \frac{Fs_0}{d} \tag{31}$$

[38] Therefore, both C_u and S_0 increase with increasing inter-particle shear resistant (Fs_0) and coefficient of friction (μ_p). Note that for a given material, F_{S0}/d is a constant; thus, C_u and S_0 are not influenced by particle diameter (d).

[39] When the lattice fails in uniaxial compressive test, the vertical strain (ε_c) is (details in Appendix A)

$$\varepsilon_c = -\frac{\sqrt{3}(K_n+3K_s)}{3K_nK_s} \cdot \frac{Fs_0}{d\left(1-\sqrt{3}\mu_p\right)} \tag{32}$$

[40] In conclusion, the five mechanical properties of the close-packed model, Young's modulus (E), Poisson's ratio (v), tensile strength (T_u), compressive strength (C_u), and coefficient of intrinsic friction (μ_i) can be defined by the five inter-particle parameters, normal stiffness (K_n), shear stiffness (K_s), breaking displacement (X_b), shear resistance (Fs_0), and coefficient of friction (μ_p). The conversion formulas between material properties and particle parameters are provided in Appendices B and C.

5. Examples and Validations

5.1. Close-Packed Lattices of Quartz

[41] A MATLAB code "MatDEM" has been developed on the basis of the model introduced in this paper. Numerical models of quartz were used as an example to validate the formulas and test the errors derived from particle number (mesh density) and magnitude of strain. As *Boutt and McPherson* [2002], we do not stipulate a single particle to represent a single rock grain, but rather, the assemblage represents a collection of spatially averaged grains. The mechanical properties of the quartz and corresponding inter-particle parameters are shown in Table 1. The particle diameter (d) is 0.001 m, and the particle mass (M_p) is 2.295×10^{-3} kg according to the following equation [*Hardy and Finch*, 2006]:

$$M_p = \rho \cdot \left(\sqrt{3}d^2/2\right) \tag{33}$$

where ρ is the density of quartz, which is 2.650×10^3 kg/m^3.

[42] The particle parameters were used to define a series of close-packed lattices, of which the aspect ratios (height/width) were about 1. The particle numbers of the lattices along the horizontal direction (N) are 2, 4, 8, 15, 30, 60, and 120 (i.e., 0.2 mm to 120 mm in width), and corresponding particle numbers are, respectively, 3 (single unit), 18, 68, 247, 1033, 4106, and 16,611. In numerical simulations, the lattices experienced tensile stress or compressive stress to test the mechanical properties of the lattices. As shown in Figure 1a, the lattice is bonded by two smooth planes respectively on the top and bottom sides. Only normal forces act on boundary particles, and there is no friction between the particles and the two planes.

5.2. Tests of Elastic Properties

[43] The elastic properties of the lattice can be computed via compressive tests. As shown in Figure 1a, 68 particles

Table 1. Quartz mechanical properties [*Pollard and Fletcher*, 2005, pp. 321, 343, and 361] and corresponding inter-particle parameters (particle diameter is 0.001 m)

Mechanical properties of quartz		Inter-particle parameters of lattice	
Young's Modulus (E)	90 GPa	Normal stiffness (K_n)	65.87 G N/m
Poisson's ratio (v)	0.16	Shear stiffness (K_s)	23.71 G N/m
Uniaxial tensile strength (T_u)	25 MPa	Breaking displacement (X_b)	1.901×10^{-7} m
Uniaxial compressive strength (C_u)	252 MPa	Shear resistance (Fs_0)	36.90 KN
Coefficient of intrinsic friction (μ_i)	1	Friction coefficient (μ_p)	0.2391

are bonded to form a lattice that approximates a square shape. In the numerical tests of elastic properties, top and bottom planes are moved toward the center of the lattice step by step at a speed of about 6×10^{-10} m/step (compressive step). In response to the compressive force (Fy) between them, the lattice is compressed and dilated laterally. The vertical stress (σ_{yy}) is calculated from Fy, and horizontal stress (σ_{xx}) is zero. The vertical strain (ε_{yy}) and horizontal strain (ε_{xx}) are calculated on the basis of the displacement of the particles. Then, the shear modulus (G) and the Lame's constant (λ) are calculated from equation (14), with which the Young's modulus (E) and Poisson's ratio (v) can be determined. The step time of the simulations is 2×10^{-8} s (time step). As the planes are moved very slowly and step time is very small, the calculations are performed in a quasi-static manner.

[44] When the lattice is compressed, an artificial viscosity (η) is used to avoid buildup of kinetic energy, which is determined by the following semi-empirical formula:

$$\eta = \sqrt{8 M_p K_n}/N \tag{34}$$

where M_p is the particle mass, K_n is the inter-particle normal stiffness, and N is the particle number of the square lattice along the horizontal direction ($N = 2, 4, 8, \ldots, 120$). According to a series of numerical tests, the kinematic energy of the square lattice reduces at a high speed using the viscosity defined by equation (34). After each compressive step, the simulation is run for 400 time steps in order to damp reflected waves from the two edges of the lattice. As a result, the kinematic energy is almost zero when a new compressive step starts.

[45] A series of numerical tests was conducted to quantify the errors of the lattice elastic properties. The E and v of the lattices with different particle numbers and different vertical strains are plotted, respectively, in Figures 6a and 6b. The curves of three particles (black dashed lines) correspond to the single triangle unit of Figure 2. As shown in Figure 6a, when the vertical strain is very small, the tested E and v are very close to the values of real quartz, 90 GPa and 0.16, respectively. The lattice with 18 particles has the lowest precision: Young's modulus is about 3% lower than the theoretical value. When the particle number increases, the elastic properties of the lattice converge to the theoretical values.

[46] Under compressive stress, Young's modulus decreases and Poisson's ratio increases with increasing magnitude of the vertical strain. The elastic properties almost maintain constant values when the magnitude of strain is lower than 10^{-3}. When the magnitude of strain exceeds 10^{-3}, the Young's modulus decreases and the Poisson's ratio increases significantly. Note that if a tensile stress is applied to the lattice, the Young's modulus will increase and the Poisson's ratio will decrease with increasing magnitude of vertical strain.

[47] In the model, it is assumed that the unit remains an equilateral triangle shape when it is compressed. When the vertical strains are very small, the simulated values are close to the theoretical values (Figures 6a and 6b). However, when the vertical strain is great, the unit cannot be regarded as an equilateral triangle. As the unit dilates laterally, the calculated vertical stress and Young's modulus will be lower. When the vertical strain is -10^{-3}, the simulated Young's modulus and Poisson's ratio of one unit are, respectively, 0.034% lower and 0.084% greater than corresponding theoretical values.

5.3. Tests of Strengths

[48] In the numerical simulations of compressive and tensile strength tests, all particles of a lattice were originally bonded to their neighbors and deformed elastically. Then, the lattices were compressed step by step at a speed of 1.90×10^{-9} m/step or extended at a speed of 1.90×10^{-10} m/step, until the lattices failed. The time step and viscosity used in the tests of compressive strength and tensile strength are the same as those of the elastic tests. The numerical simulations were performed using a quadcore CPU workstation, which has a peak performance of about 48 Gflops. For the largest lattice with 16,611 particles, the simulation was run for 8×10^4 compressive steps and a total of 3.2×10^7 time steps, which took 409 h CPU time.

[49] The stress path of a lattice with 1033 particles is illustrated in Figure 7a. The vertical stress increases linearly from the origin O until reaching point A, where tensile

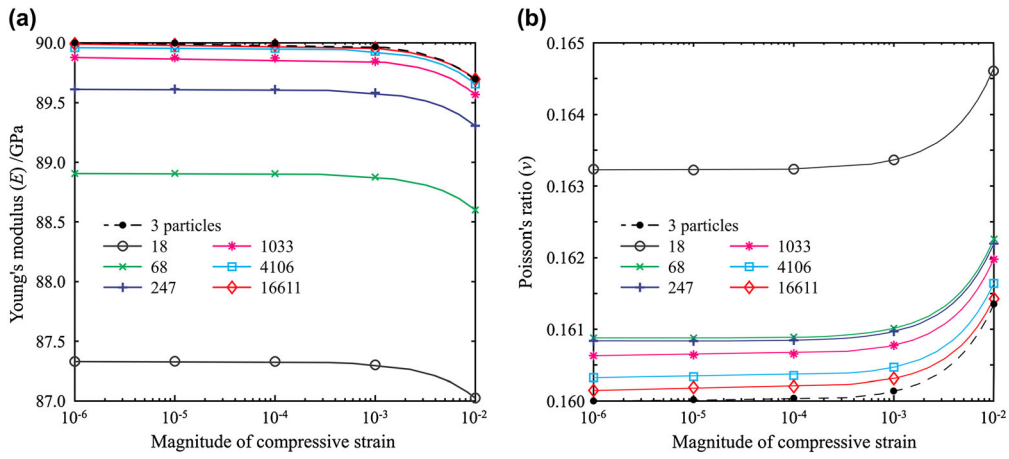

Figure 6. Test results for Young's modulus and Poisson's ratio of one unit (three particles) agree with the theoretical values, 90 GPa and 0.16, respectively. Deviations of elastic properties of other lattices increase with the increasing magnitude of strain and decrease with increasing particle number. (a) Young's modulus; (b) Poisson's ratio.

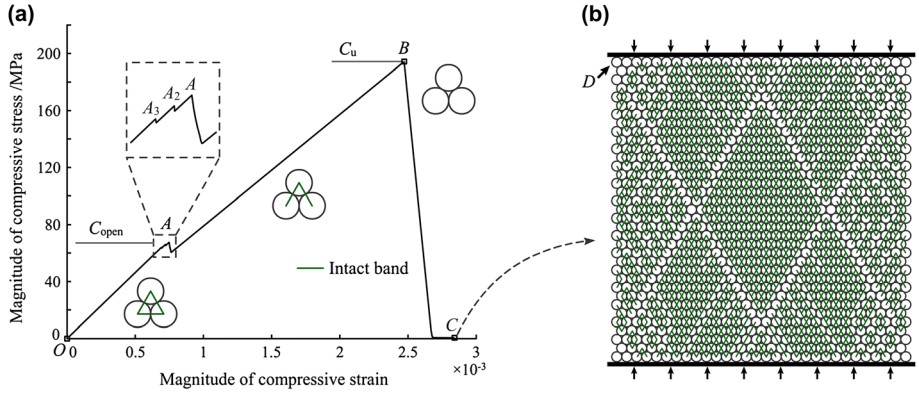

Figure 7. (a) Stress-strain graph of lattice with 1033 particles (30 particles along horizontal direction). Opening micro-cracks appear when the compressive stress reaches C_{open}. The peak value of the curve is the uniaxial compressive strength (C_u). (b) The lattice status at point C of the stress-strain graph. Note: line segments between particles represent intact bonds.

micro-cracks formed, and as a result, the stress declines a bit. Then, the stress increases almost linearly, but the rate is lower than that of OA. The whole lattice fails when the stress reaches the uniaxial compressive strength (C_u) at point B. Then the stress drops dramatically to almost zero at point C. The lattice at point C is shown in Figure 7b. Two obvious "X" shear zones appear in the failed lattice [*Antonellini and Pollard*, 1995; *Hardy et al*., 2009], which are similar to the conjugate shear fractures observed in some compressive tests on rock [*Borg and Handin*, 1966; *Wong et al*., 2001]. The phenomenon of the numerical test coincides with that of previous experimental tests using specimens of fine-grained quartzite [*Hallbauer et al*., 1973]. In this experiment, the first visible structural damage appears as elongated opening micro-cracks having their axes oriented parallel to the direction of maximum compressive stress. Then, the number of micro-cracks increased drastically and finally link up to form a macroscopic shear plane.

[50] The simulated C_u was calculated for a series of lattices with particle numbers from 3 to 16,611, and the results are plotted in Figure 8a. Similar to the compressive tests, the tensile tests of the seven lattices were simulated and the results are plotted in Figure 8b. As shown in the two figures, the C_u and T_u of one unit (three particles) are, respectively, 0.98% and 0.03% lower than the theoretical values (dashed lines). For one unit, the failure strain of the C_u test (3.17×10^{-3}) is about 10 times greater than that of the T_u test (2.71×10^{-4}). As indicated in Figure 6, the errors of the elastic properties increase dramatically when the strain exceeds 10^{-3}. Therefore, the error of C_u is much greater than the error of T_u.

[51] The simulated compressive strength and tensile strength are much smaller than theoretical values for other lattices with multiple units. The average error of C_u for the other six lattices (18–16611 particles) is about 22.2%, and the error of T_u is about 4.3%. The greater errors are due to "boundary effects" and stress concentrations. As shown in Figure 7b, only one particle holds up the particle D on its bottom side. When the lattice is compressed, the displacement of particle D is greater in comparison with other neighboring particles. As a result, the boundary particle will break earlier, and stress will concentrate on nearby particles, which then break. As shown in Figure 7a, the stress drops a bit at points A_2 and A_3 prior to the point A, which indicates that some boundary bonds break earlier. Furthermore, the amount of broken bonds is much greater near the left and right sides of the lattice, in particular, near the four corners (Figure 7b). Therefore, the simulated C_u and T_u of lattices with multiple units are much smaller than the theoretical values.

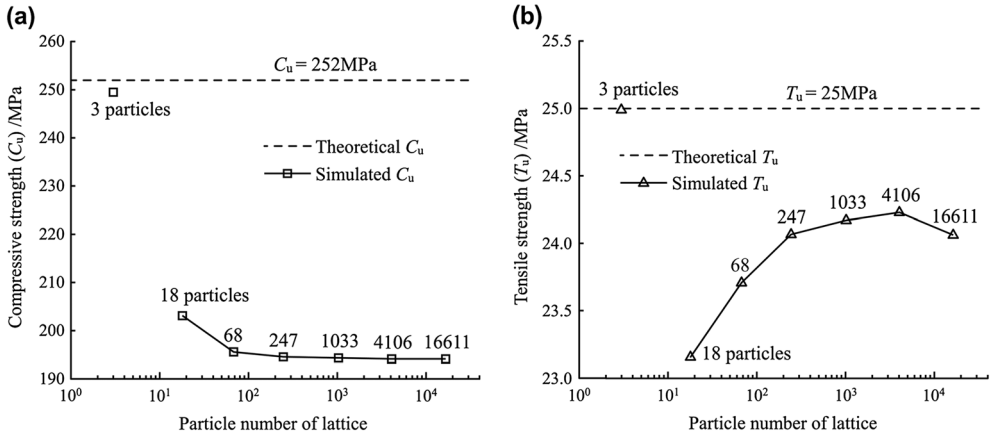

Figure 8. (a) Simulated uniaxial compressive strength (C_u) and (b) tensile strength (T_u) with different particle numbers. Dashed lines are corresponding theoretical values.

6. Discussions and Conclusions

[52] Traditionally, the creation of discrete element model with specified mechanical properties relies on calibration processes to determine the correct inter-particle parameters. In this paper, the rock was represented by bonded particles to investigate the dependence of rock mechanical properties on inter-particle parameters of the lattice model. Five parameters were used to define the inter-particle properties of the lattice, including normal stiffness (K_n), shear stiffness (K_s), breaking displacement (X_b), shear resistance (Fs_0), and coefficient of friction (μ_p). Based on the assumption of small deformation, the conversion formulas between micro inter-particle parameters and macro-material properties were derived. With the application of the model and formulas, it is easy to create material of lattice that has similar elastic properties and failure criteria to rock and crystal.

[53] Numerical models of quartz material were used to validate the formulas and test the errors derived from particle number and strain. The Young's modulus and Poisson's ratio of one unit meet the theoretical values predicted by the formulas. The errors of lattices with multiple units are greater. However, when particle number increases, the errors of the simulated values decrease and converge to corresponding theoretical values. Since the formulas is on the basis of the assumption of small deformation, the errors of elastic properties increase with increasing magnitude of strain. The errors increase significantly when the magnitude of strain is greater than 10^{-3}.

[54] In the numerical tests of uniaxial compressive strength (C_u) and tensile strength (T_u), the measured strengths are lower than theoretical values, due to the boundary effects and stress concentrations. Furthermore, as the breaking strain of uniaxial compressive test (3.17×10^{-3}) is greater than 10^{-3}, the error of uniaxial compressive strength is much greater than that of tensile strength. An alternative way to counteract the influence of the boundary effects is to use a greater C_u and T_u in the conversion formulas (Appendix B). Such as the T_u of the block with 1033 particles is 3.3% lower than the theoretical T_u; thus, it should be increased by 3.4% in the conversion formulas.

[55] The analytical solutions are applicable to a regular close-packed lattice, which is more comparable to a pure crystal, such as quartz. However, the disadvantage of the crystalline lattice is anisotropy [*Place and Mora*, 1999], and fractures tend to develop along 60° planes as shown in Figure 7b. In Figures 2 and 5, the force acting on the triangle unit is vertical, and the conversion formulas are validated along the vertical direction (90°). As the unit is centrosymmetric, the mechanical properties of the unit along the directions of 30° and 150° also follow the formulas. However, the mechanical properties of the unit along the horizontal direction may be different. Although we do not have analytical solutions of all the directions, some numerical tests indicate that the Young's modulus (E) and tensile strength (T_u) are a bit lower along other directions. The anisotropic property of the lattice can be an interesting further research topic.

[56] Random assemblies with polydisperse size distributions and random packing were usually used to counteract the influence of anisotropic in many previous studies. Fortunately, the random assemblies have been shown to have some similar elastic and failure characteristics as lattice models. For example, the solutions indicate that Poisson's ratio increases with increasing ratio of shear stiffness to normal stiffness (equation (C2)), the inter-particle coefficient of friction (μ_p) controls the slope of the Mohr-Coulomb failure envelope of the lattice (equation (27)), and C_u increases with increasing inter-particle shear resistant (Fs_0) and coefficient of friction (equation (C4)), which coincides with previous numerical tests of random assemblies. The solutions indicate how the macro-mechanical properties of lattice are influenced by the micro inter-particle parameters and consequently provide a theoretical basis for the calibration of the parameters of random assemblies. Such as, for a certain random assemblage, K_n and K_s can be used to adjust the Young's modulus and Poisson's ratio of the assemblage according to equations (C1) and (C2), respectively.

[57] At microscopic scale, rocks are composed of irregularly shaped grains, each of which can be represented by a close-packed lattice. With the application of the model and the conversion formulas introduced in this study, the grains can simulate elastic properties and failure behaviors of rocks and crystals. Then, the model can be used to simulate complicated structures that involve deformation and failure at different scales. Such as compaction bands (macroscopic) in sandstone [*Sternlof et al.*, 2005], which involve breakage of quartz grains at microscopic scale.

Appendix A: Uniaxial Compressive Strain

[58] In Figure 5, bond 2 breaks when the magnitude of compressive stress exceeds the limit of C_{open}. Then, the balances of particle 1 along vertical direction and particle 2 along horizontal direction require that

$$\begin{cases} -Fy = -\sqrt{3}\cdot F_{n1} - F_{S1} \\ -1/2\cdot F_{n1} = -Fx - \sqrt{3}/2\cdot F_{S1} \end{cases} \tag{A1}$$

[59] Equation (24) can be derived from equation (A1). The physical equations and geometrical equations are

$$\begin{cases} F_{n1} = K_n\cdot X_{n1} \\ F_{S1} = K_s\cdot X_{s1} \end{cases} \tag{A2}$$

$$\begin{cases} X_{n1} = \sqrt{3}/2\cdot dy + 1/4\cdot X_{n2} \\ X_{s1} = 1/2\cdot dy - \sqrt{3}/4\cdot X_{n2} \end{cases} \tag{A3}$$

[60] With equations (A1) and (A2), the solution of vertical displacement (dy) is

$$dy = (K_n + 3K_s)/(8K_nK_s)\cdot Fy \tag{A4}$$

[61] According to equation (29), when bond 1 breaks, the vertical compressive force (Fy) is

$$Fy = -C_u\cdot d = -\frac{4}{1-\sqrt{3}\mu_d}\cdot F_{S0} \tag{A5}$$

[62] With equations (A4) and (A5), the corresponding vertical strain is

$$\varepsilon_c = \frac{dy}{l_{AO}} = -\frac{\sqrt{3}(K_n + 3K_s)}{3K_nK_s} \cdot \frac{F_{S0}}{d\left(1 - \sqrt{3}\mu_d\right)} \tag{A6}$$

Appendix B: Conversion Formulas of Material Properties to Inter-particle Parameters

[63] Inter-particle normal stiffness (K_n), shear stiffness (K_s), breaking displacement (X_b), shear resistance (Fs_0), and coefficient of friction (μ_p) can be defined by

$$K_n = \frac{E}{\sqrt{3}(1-2\nu)\cdot(1+\nu)} \tag{B1}$$

$$K_s = \frac{E(1-4\nu)}{\sqrt{3}(1-2\nu)\cdot(1+\nu)} \tag{B2}$$

$$X_b = \frac{2K_n + K_s}{2\sqrt{3}K_n(K_n + K_s)} \cdot T_u \cdot d \tag{B3}$$

$$F_{S0} = \left(1/4 - \sqrt{3}/4 \cdot \mu_p\right) \cdot C_u \cdot d \tag{B4}$$

$$\mu_p = \frac{-3\sqrt{3} + \sqrt{3}I}{3 + 3I}, I = \left[\left(1 + \mu_i^2\right)^{1/2} + \mu_i\right]^2 \tag{B5}$$

Appendix C: Conversion Formulas of Inter-particle Parameters to Material Properties

[64] Young's modulus (E), Poisson's ratio (ν), tensile strength (T_u), compressive strength (C_u), and coefficient of intrinsic friction (μ_i) can be expressed as

$$E = \sqrt{3}(K_n + K_s)\cdot(5K_n - K_s)/(8K_n) \tag{C1}$$

$$\nu = 1/4\cdot(1 - K_s/K_n) \tag{C2}$$

$$T_u = {}^u 2\sqrt{3}K_n(K_n + K_s) \cdot \frac{X_b}{d} \tag{C3}$$

$$C_u = \frac{4}{1 - \sqrt{3}\mu_p} \cdot \frac{F_{S0}}{d} \tag{C4}$$

$$\mu_i = \frac{P-1}{2\sqrt{P}}, P = \frac{3 + \sqrt{3}\mu_p}{1 - \sqrt{3}\mu_p} \tag{C5}$$

[65] **Acknowledgments.** Financial support from the Rock Fracture Project of Stanford University, Natural Science Foundation of China (No.41272315) and the National Basic Research Program of China (973 Program, No. 2011CB710605) is gratefully acknowledged. We are grateful to anonymous reviewers for many valuable suggestions that notably improved the manuscript.

References

Antonellini, M., and D. Pollard (1995), Distinct element modeling of deformation bands in sandstone, *Journal of Structural Geology*, *17*(8), 1165–1182.

Bathurst, R., and L. Rothenburg (1988), Note on a random isotropic granular material with negative Poisson's ratio, *International Journal of Engineering Science*, *26*(4), 373–383.

Benesh, N., A. Plesch, J. Shaw, and E. Frost (2007), Investigation of growth fault bend folding using discrete element modeling: Implications for signatures of active folding above blind thrust faults, *Journal of Geophysical Research-Solid Earth*, *112*, B03S04.

Boutt, D., and B. McPherson (2002), Simulation of sedimentary rock deformation: Lab-scale model calibration and parameterization, *Geophysical Research Letters*, *29*(4), 1054.

Borg, I., and J. Handin (1966), Experimental deformation of crystalline rocks, *Tectonophysics*, *3*(4), 249–367.

Carmona, A., R. Clavera-Gispert, O. Gratacos, and S. Hardy (2010), Modelling syntectonic sedimentation: Combining a discrete element model of tectonic deformation and a process-based sedimentary model in 3D, *Mathematical Geosciences*, *42*(5), 519–534.

Cundall, P., and O. Strack (1979), A discrete element model for granular assemblies, *Geotechnique*, *29*(1), 47–65.

Ergenzinger, C., R. Seifried, and P. Eberhard (2011), A discrete element model to describe failure of strong rock in uniaxial compression, *Granular Matter*, *13*(4), 341–364.

Finch, E., S. Hardy, and R. Gawthorpe (2003), Discrete element modelling of contractional fault-propagation folding above rigid basement fault blocks, *Journal of Structural Geology*, *25*(4), 515–528.

Gaspar, N. (2010), A granular material with a negative Poisson's ratio, *Mechanics of Materials*, *42*(7), 673–677.

Griffith, A. (1921), The phenomena of rupture and flow in solids, *Philosophical Transactions of the Royal Society of London*, *221*, 163–198.

Griffiths, D., and G. Mustoe (2001), Modelling of elastic continua using a grillage of structural elements based on discrete element concepts, *International Journal For Numerical Methods in Engineering*, *50*(7), 1759–1775.

Hallbauer, D., H. Wagner, and N. Cook (1973), Some observations concerning the microscopic and mechanical behaviour of quartzite specimens in stiff, triaxial compression tests, *International Journal of Rock Mechanics and Mining Sciences*, *10*(6), 713–726.

Hardy, S., and E. Finch (2005), Discrete-element modelling of detachment folding, *Basin Research*, *17*(4), 507–520.

Hardy, S., and E. Finch (2006), Discrete element modelling of the influence of cover strength on basement-involved fault-propagation folding, *Tectonophysics*, *415*(1–4), 225–238.

Hardy, S., and E. Finch (2007), Mechanical stratigraphy and the transition from trishear to kink-band fault-propagation fold forms above blind basement thrust faults: A discrete-element study, *Marine and Petroleum Geology*, *24*(2), 75–90.

Hardy, S., K. McClay, and J. Munoz (2009), Deformation and fault activity in space and time in high-resolution numerical models of doubly vergent thrust wedges, *Marine and Petroleum Geology*, *26*(2), 232–248.

Hazzard, J., R. Young, and S. Maxwell (2000), Micromechanical modeling of cracking and failure in brittle rocks, *Journal of Geophysical Research-Solid Earth*, *105*(B7), 16683–16697.

Hoover, W., W. Ashurst, and R. Olness (1974), Two-dimensional Computer Studies of Crystal Stability and Fluid Viscosity, *Journal of Chemical Physics*, *60*(10), 4043–4047.

Horii, H., and S. Nemat-Nasser (1985), Compression-induced microcrack growth in brittle solids: Axial splitting and shear failure, *Journal of Geophysical Research-Solid Earth and Planets*, *90*(NB4), 3105–3125.

Kazerani, T., and J. Zhao (2010), Micromechanical parameters in bonded particle method for modelling of brittle material failure, *International Journal For Numerical and Analytical Methods in Geomechanics*, *34*(18), 1877–1895.

Kruyt, N.P., and L. Rothenburg (2004), Kinematic and static assumptions for homogenization in micromechanics of granular materials, *Mechanics of Materials*, *36*, 1157–1173.

Kuhn, M. (1999), Structured deformation in granular materials, *Mechanics of Materials*, *31*(6), 407–429.

Kuhn, M., and K. Bagi (2004), Contact rolling and deformation in granular media, *International Journal of Solids and Structures*, *41*(21), 5793–5820.

Lakes, R. (1987), Foam structures with a negative Poisson's ratio, *Science*, *235*(4792), 1038–1040.

Malan, D., and J. Napier (1995), Computer modelling of granular material microfracturing, *Tectonophysics*, *248*(1–2), 21–37.

Mei, Z., Y. Liu, and H. Yang (1999), Research on a new remeshing method for the 3D FEM simulation of blade forging, *Journal of Materials Processing Technology*, *94*(2–3), 231–234.

Moore, D., and D. Lockher (1995), The role of microcracking in shear fracture propagation in granite, *Journal of Structural Geology*, *17*(1), 95–114.

Mora, P., and D. Place (1993), A lattice solid model for the non-linear dynamics of earthquakes, *International Journal of Modern Physics C-Physics and Computers*, *4*(6), 1059–1074.

Mora, P., and D. Place (1994), Simulation of the frictional stick-slip instability, *Pure and Applied Geophysics*, *143*(1–3), 61–87.

Morgan, J., and M. Boettcher (1999), Numerical simulations of granular shear zones using the distinct element method—1. *Shear zone kinematics and the micromechanics of localization, Journal of Geophysical Research-Solid Earth*, *104*(B2), 2703–2719.

Nitka, M., G. Combe, C. Dascalu, and J. Desrues (2011), Two-scale modeling of granular materials: A DEM-FEM approach, *Granular Matter*, *13*(3), 277–281.

Paluszny, A., and S.K. Matthai (2009), Numerical modeling of discrete multi-crack growth applied to pattern formation in geological brittle media, *International Journal of Solids and Structures*, *46*(18–19), 338–3397.

Place, D., and P. Mora (1999), The lattice solid model to simulate the physics of rocks and earthquakes: Incorporation of friction, *Journal of Computational Physics*, *150*(2), 332–372.

Place, D., F. Lombard, P. Mora, and S. Abe (2002), Simulation of the micro-physics of rocks using LSMearth, *Pure and Applied Geophysics*, *159*(9), 1911–1932.

Pollard, D., and R. Fletcher (2005), Fundamentals of Structural Geology, Cambridge University Press, United Kingdom.

Potyondy, D., and P. Cundall (2004), A bonded-particle model for rock, *International Journal of Rock Mechanics and Mining Sciences*, *41*(8), 1329–1364.

Roul, P., A. Schinner, and K. Kassner (2011), Mechanical properties of non-cohesive polygonal particle aggregates, *Granular Matter*, *13*(4), 303–317.

Saltzer, S., and D. Pollard (1992), Distinct element modeling of structures formed in sedimentary overburden by extensional reactivation of basement normal faults, *Tectonics*, *11*(1), 165–174.

Sternlof, K., J. Rudnicki, and D. Pollard (2005), Anticrack inclusion model for compaction bands in sandstone, *Journal of Geophysical Research-Solid Earth*, *110*, B11403.

Tavarez, F., and M. Plesha (2007), Discrete element method for modelling solid and particulate materials, *International Journal For Numerical Methods in Engineering*, *70*(4), 379–404.

Tradegard, A., F. Nilsson, and S. Ostlund (1998), FEM-remeshing technique applied to crack growth problems, *Computer Methods in Applied Mechanics and Engineering*, *160*(1–2), 115–131.

Wang, B., Y. Chen, and T. Wong (2008), A discrete element model for the development of compaction localization in granular rock, *Journal of Geophysical Research-Solid Earth*, *113*, B03202.

Wensrich, C., and R. Stratton (2011), Shock waves in granular materials: Discrete and continuum comparisons, *Powder Technology*, *210*(3), 288–292.

Wong, T.-F., P. Baud, and E. Klein (2001), Localized failure modes in a compactant porous rock, *Geophysical Research Letter*, *28*, 2521–2524.

Yin, H., J. Zhang, L. Meng, Y. Liu, and S. Xu (2009), Discrete element modeling of the faulting in the sedimentary cover above an active salt diapir, *Journal of Structural Geology*, *31*(9), 989–995.